THE REBOUND OF NON-SPHERICAL PARTICLES IN GAS TURBINE COMPONENTS

Jack G. Gaskell, Matthew McGilvray, David R. H. Gillespie

Oxford Thermofluids Institute, Department of Engineering Science, University of Oxford, Oxford OX1 3UJ, UK

ABSTRACT

Particulate deposition can cause significant damage to gas turbine components. Modelling the location and quantity of deposition is desirable to optimise component geometry and quantify cost of ownership effects that arise from the ingestion of atmospheric contaminants. Bounce-stick modelling predicts whether a particle will bounce, stick or shatter upon impact with a wall. Current modelling assumes that particles are spherical, which is not the case for real atmospheric particulates. This paper uses FEA to examine the sensitivity of particle rebound trajectories to non-sphericity and characterise the collision physics of spheroids. Rebound trajectories are shown to differ significantly from those of equivalent spheres with a strong dependence on particle orientation. Significant angular velocities are observed upon rebound, which vary in both sign and magnitude with the potential to affect downstream trajectories through the Magnus force. Future bounce-stick models should include the effects of non-sphericity to accurately predict rebound trajectories and downstream deposition.

KEYWORDS

Particles, Bounce-Stick, Gas Turbines, Deposition, Sand.

NOMENCLATURE

τ_p^+ Non-dimensional particle relaxation time from Marchioli, Fantoni, and Soldati, 2010

$\mathrm{CoR_n}$, $\mathrm{CoR_t}$ Normal and tangential coefficients of restitution, $|V_{\mathrm{n2}}/V_{\mathrm{n1}}|$ and $V_{\mathrm{t2}}/V_{\mathrm{t1}}$

θ_i, θ Particle impingement and orientation angles, $^\circ$

θ_x Component of particle orientation angle θ from Marchioli, Fantoni, and Soldati, 2010

A_{proj} Particle maximum projected area, m^2

AR, Sh Particle Aspect Ratio and Shape Factor

D_{p} Particle equivalent spherical diameter, m

L_{proj} Particle maximum projected length, m

M_{fric}, M_{rebound} Particle centroid moments due to friction and non-spherical geometry, Nm

P Particle perimeter, m

V_{i}, V_{n1} & V_{t1} Particle initial total, normal and tangential velocities, ms^{-1}

y^+ Dimensionless wall distance, defined by friction velocity (Marchioli, Fantoni, and Soldati, 2010)

INTRODUCTION

Ingested atmospheric particulates are known to cause significant damage to gas turbine components, notably through deposition in the secondary air system and turbine blade cooling passages (Dunn, 2012). The reduction in flow capacity and corrosion that often results are a major driver of in-service maintenance costs. The ability to accurately model deposition would enable the design of more durable components and better predictions of maintenance requirements.

Bounce-stick models are used to determine whether a particle bounces, sticks or shatters upon impact with a wall. They may also predict the trajectory of rebound by providing values of coefficient of restitution (CoR), the ratio of outbound to inbound linear velocity components. Where a sphere collides with a smooth substrate, the impact is assumed to be as defined in Figure 1. Existing bounce-stick models, notably (Bons, Prenter, and Whitaker, 2017; Yu and Tafti, 2019; Brach and Dunn, 1992) assume that particles are cylindrical or spherical to reduce the mathematical complexity of their approaches. However, there is little published literature on the sensitivity of particle rebound to non-sphericity typical of real ingested particulates. A simple soft-sphere type approach was used by Wynn (2009) to model the rebound of spheroids, finding that multiple bounces may occur and that rebound becomes more distinct from that of a sphere with increasing non-sphericity. Stochastic corrections for non-sphericity have also been developed (Whitaker and Bons, 2018), however they are necessarily limited to the specific particle shapes, sizes and materials tested without modelling the underlying collision physics.

Reid (2003) describes the composition and morphology of atmospheric contaminants sampled between ground level and 5000 m altitude. The dust was collected over Puerto Rico having originated in Africa, the world's largest source of mineral dust (Chou et al., 2008). Particle morphology did not vary significantly with altitude and all particles were characterised as prolate spheroids using two primary parameters: aspect ratio (AR) and shape factor (Sh) as described in Equations 1 and 2:

$$AR = \frac{\pi L_{\text{proj}}^2}{4A_{\text{proj}}} \tag{1}$$

$$Sh = \frac{P^2}{4\pi A_{\text{proj}}} \tag{2}$$

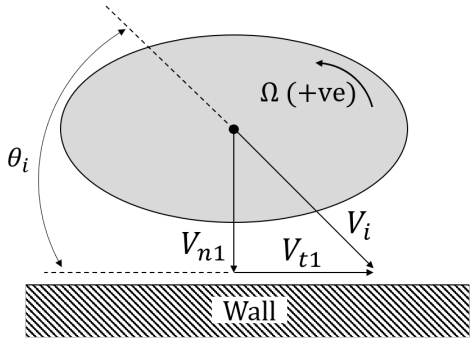

Figure 1: Particle sign convention

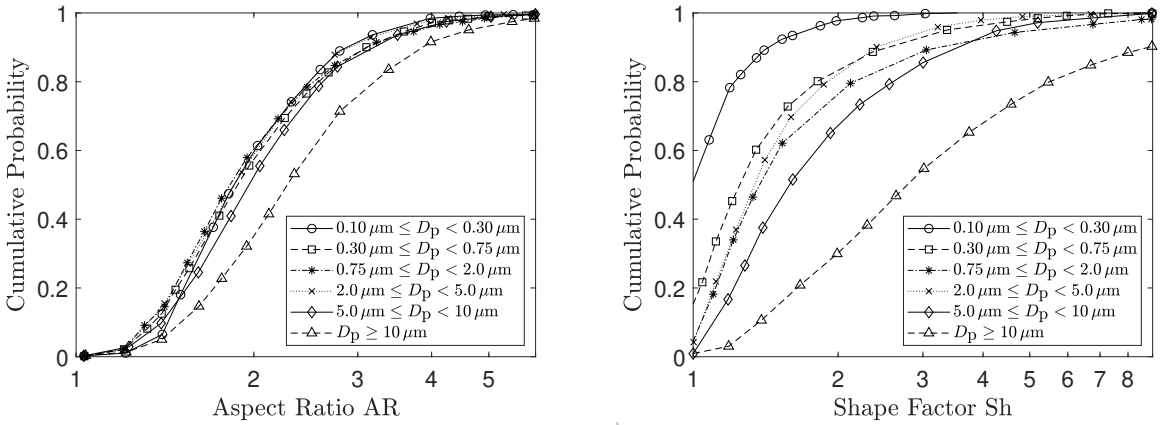

(a) **(b)**

Figure 2: Airborne particulate morphology from Reid (2003)

Approximating the shape of real particulates as prolate spheroids, the Aspect Ratio (AR) is the best fit ratio of major to minor axis lengths while shape factor is a measure of particle roundness where values greater than unity describe a more "jagged" shape. Aspect ratio did not vary significantly with particle diameter with a median value of 1.9 and standard deviation of 0.9 as shown in Figure 2a, similar to the values reported in (Chou et al., 2008). Particle shape factor did vary significantly with size, as shown by Figure 2b. Higher particle surface roughness will likely increase plastic deformation and lower the normal coefficient of restitution. However, to study the bulk effects of non-sphericity only the effects of aspect ratio will be considered in the present work.

Previous workers have shown through DNS that non-spherical particles behave differently in near-wall turbulence when compared to spheres. The wall-normal velocities of inertial elongated fibres, studied by Marchioli, Fantoni, and Soldati (2010), are affected by both aspect ratio and inertia. Non-monotonic variations of wall-normal velocity are observed with changing AR and particle relaxation time τ_p^+. This behaviour is explained by the rate at which the particles are centrifuged out of near-wall vortex cores due to inertia and attain different positions on the vortex periphery based on their elongation, thus "seeing" different local flowfields. This effect is shown by a greater relative concentration of higher aspect ratio particles near the wall. This translates into a greater likelihood of higher aspect ratio particles colliding with the wall across all values of τ_p^+ considered. Marchioli, Fantoni, and Soldati (2010) also studied the preferential orientation of spheroids near the wall, finding that spheroids with a higher aspect ratio were more likely to orient their long axes with the mean streamwise direction in turbulent channel flow, as shown by Figure 3. This implies that real particles are more likely to "tumble" end-over-end when colliding with the wall, rather than to "log-roll". This matches the findings of Jie et al. (2019) who also propose an explanation for the phenomenon, related to fluid Lagrangian stretching and compression. Therefore, it is known that anisotropic particles are more likely to collide with a wall than their spherical equivalents and that they are more likely than not to collide while tumbling: the manner most distinct from spheres. This configuration is used in the present work, with the spheroids' major axis and velocity vectors in the plane normal to the wall.

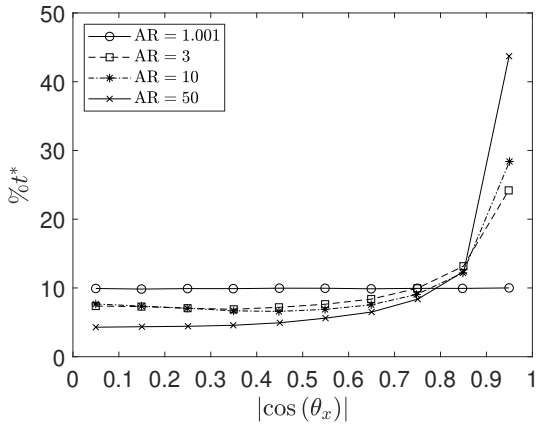

(a) $\tau_p^+ = 1$

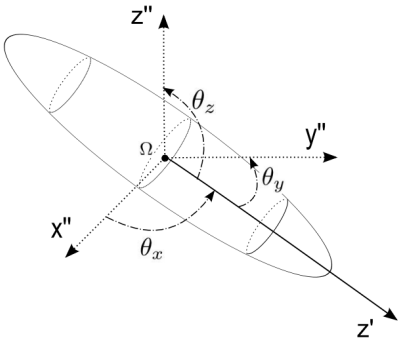

(b) Particle orientation sign convention, x'' is the mean streamwise direction

Figure 3: From Marchioli, Fantoni, and Soldati (2010). Percentage of time that particles spend with a given orientation, where dimensionless wall distance $\mathrm{y}^+ < 10$

Where a particle rebounds from a surface, bounce-stick models predict the outbound trajectory. Where multiple bounces occur, the effect of collisions on downstream trajectory will determine where or if deposition occurs. The angular velocity and position in the boundary layer of rebounding micron-scale particulates was shown by Gaskell et al. (2020) to significantly affect the trajectory of rebounding spheres through the Magnus force: CFD of a secondary air system-representative duct showed instances of up to 35% of injected particulates depositing with collision-induced rotation (CIR) while none deposited where the CIR model was disabled. Therefore, deviations in particle angular velocity and trajectory due to non-sphericity could significantly affect the likelihood of subsequent wall collisions.

The present work aims to determine the sensitivity of particle rebound trajectory to non-sphericity, considering geometries relevant to the particles ingested by gas-turbines. It also aims to describe how the collision dynamics of spheroids differ from those of spheres to aid in the development of bounce-stick models that capture particle non-sphericity.

METHOD

Airborne particulates can be characterised as prolate spheroids defined by an aspect ratio, Equation 1. Here, ANSYS Mechanical 19.2 is used to simulate the collision between alumina particles and a flat plate. Two angles characterise the configuration of the spheroid: the impingement angle θ_i and the orientation angle θ. The impingement angle is defined as in Figure 1 and denotes the angle of the particle's incoming velocity vector relative to the surface. The orientation angle describes the offset between the spheroid's long axis and the ground plane, defined where the ground plane is line $\overline{AB}$ in Figure 4a. Orientation angle is defined as negative to keep with a counterclockwise-positive sign convention in Figure 4a. The rebound of a prolate spheroid with $AR = 1.9$, the average value from Reid (2003) for airborne particulates near ground level, is compared with a sphere of equivalent volume. Two different particle incidence angles are considered, $\theta_i = 5°$ and $\theta_i = 45°$ with a range of particle orientation angles, between $\theta = 0°$ and $\theta = -180°$. Airborne particulates at the compression system exit of gas turbines have

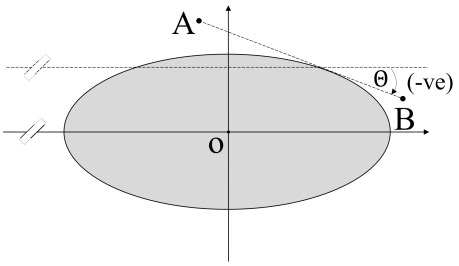

(a) Spheroid sign convention where $\overline{\mathbf{AB}}$ is the ground plane

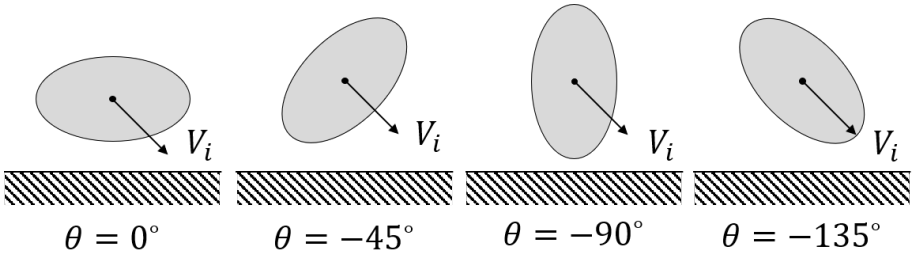

(b) Examples of different particle orientation, arrows show particle initial total velocity $\mathbf{V_i}$

Figure 4: Particle orientation sign convention

an average diameter of 6 μm (Clarkson, Majewicz, and Mack, 2016) with a range of material compositions, however millimetre-scale particles are studied here to enable validation against experimental data from (Gorham and Kharaz, 2000). This also decouples adhesive effects from spheroidal collision dynamics as particles much greater than $10\,\mu$m in diameter do not experience strong adhesive effects (Whitaker and Bons, 2018).

The alumina particles have an equivalent spherical diameter of $5\,\mathrm{mm}$ and collide with an Al2024 substrate at $V_\mathrm{i} = 3.9\,\mathrm{ms}^{-1}$ to match the experimental setup of Gorham and Kharaz (2000). The impact of equivalent spheres is compared with experimental data for validation, with the same computational setup extended to spheroids. Half-plane symmetry was applied to reduce computational time with local mesh refinement at the point of impact for both the particle and substrate.

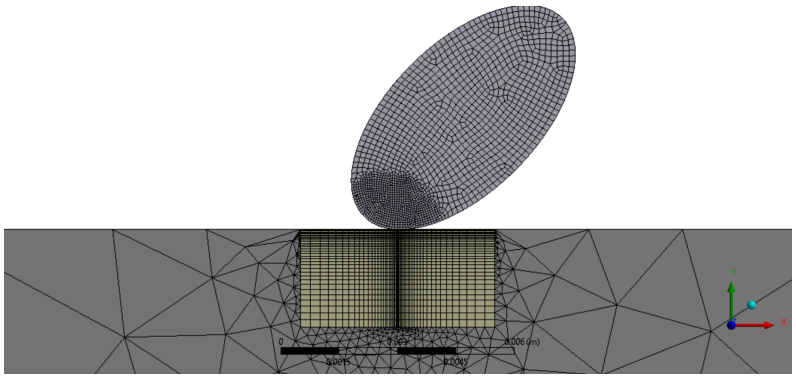

Figure 5: Mesh of $\mathrm{AR} = 1.9$ spheroid at $\theta = -45°$ with 2.75×10^5 elements

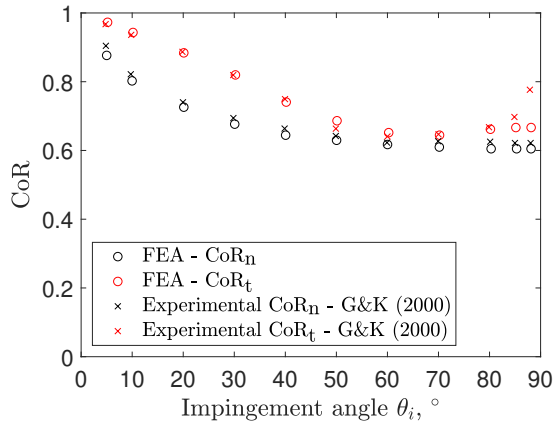

(a) Normal and tangential coefficients of restitution

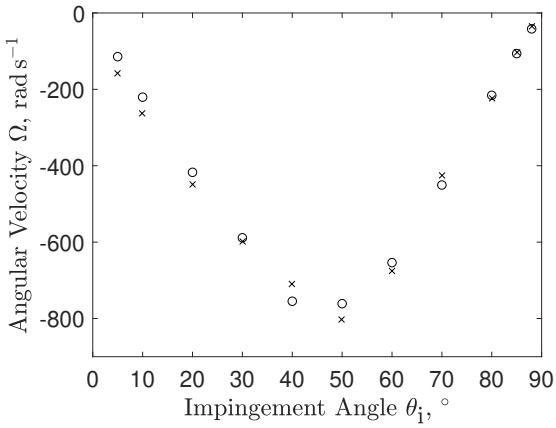

(b) Particle angular velocity post-rebound

Figure 6: FEA simulations of $\varnothing 5\,\mathrm{mm}$ alumina spheres $(\circ)$ at a range of impingement angles compared to experimental data $(\times)$ from Gorham and Kharaz (2000)

The substrate is a coupon that, without symmetry, measures $140\,\mathrm{mm} \times 140\,\mathrm{mm} \times 25\mathrm{mm}$. Hex-dominant meshing is used throughout the particle and contact region of the substrate to reduce cell count, while a tetrahedral mesh is used for the larger cells that comprise the remainder of the coupon, as shown by the contact point geometry in Figure 5.

Mesh Independence & Validation Study

FEA simulations were performed of $5\,\mathrm{mm}$ diameter spheres colliding with the substrate at $\theta_i = 50°$, matching an experimental value that was close to the mid-point between a normal and oblique collision and hence allowing comparisons between FEA and experimental data. Simulations were performed with different meshes to ensure solution independence from element size. The ratios between the sizes of elements in different regions were kept constant with the total number of elements varied between 1.55×10^5 and 5.14×10^5. A mesh with 2.78×10^5 elements was the most computationally efficient with a runtime of five hours across ten cores. Deviations of only 0.7%, 1% and 1% were recorded between the 5.14×10^5 element and 2.78×10^5 meshes for $\mathrm{CoR_n}$, $\mathrm{CoR_t}$ and Ω respectively. This number of elements or greater, with the same element size at the contact patch, was used for all subsequent simulations. Further comparison with experimental data from Gorham and Kharaz (2000) is shown in Figure 6 with good agreement between FEA and experiments. Overall, FEA is shown to accurately represent collisions of millimetre-scale particles.

RESULTS

The primary and secondary impacts of $AR = 1.9$ spheroids were simulated in FEA. For primary impacts, collisions were simulated at $\theta_i = 5°$ and $\theta_i = 45°$. Simulations of secondary collisions, where the particle re-collides with the wall shortly after the first impact, were performed using rebound trajectories from primary collisions where $\theta_i = 45°$. In all cases, rebound was defined as the point at which contact surface pressure returned to zero, indicating the particle was no longer in contact with the substrate.

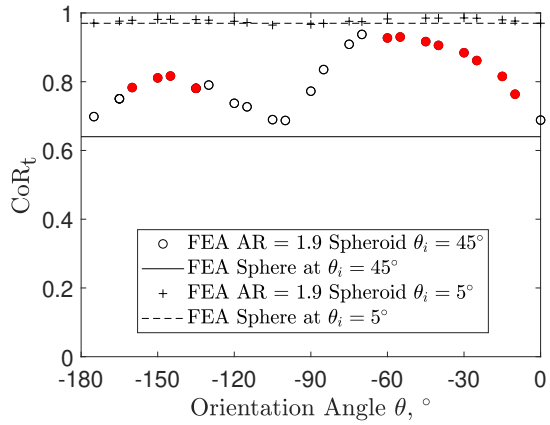

(a) Tangential coefficient of restitution

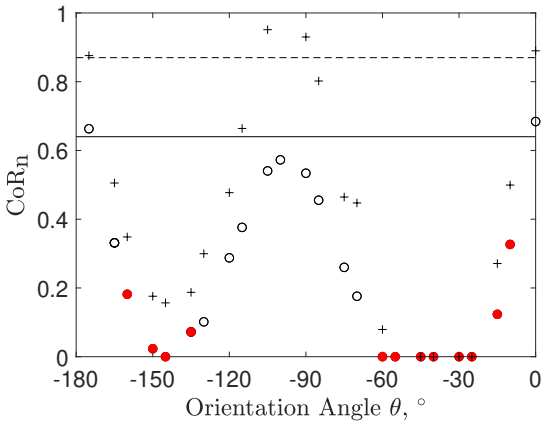

(b) Normal coefficient of restitution

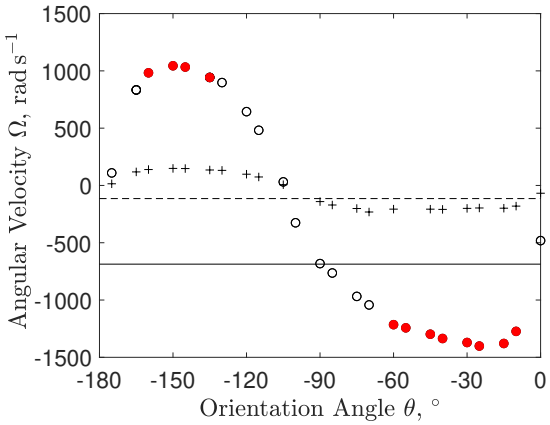

(c) Particle angular velocity post-rebound

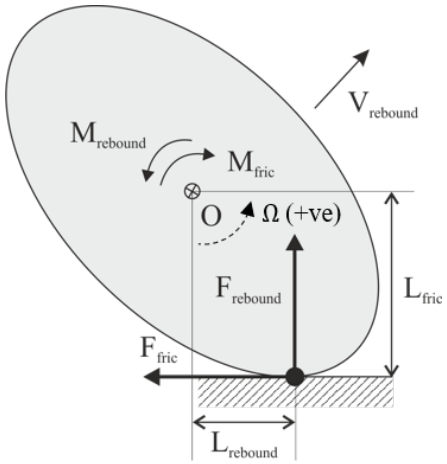

(d) Schematic of spheroid rebound at $\theta = -135°$

Figure 7: The rebound of $\mathrm{AR} = 1.9$ spheroids following primary collisions at a range of orientation angles, θ_i is $45°$ or $5°$. Red data points indicate a second collision occurs

Primary Collisions

The rebound properties of the $AR = 1.9$ spheroid at different orientation angles relative to the surface are shown in Figure 7. All values are taken at the point of rebound following the first bounce, so do not show the effect of multiple bounces occurring as described in the following subsection. Where a secondary collision occurs, the primary impact is highlighted red.

The collision kinematics of a prolate spheroid are shown schematically in Figure 7d. Both a sphere and a spheroid experience a moment about their centroids due to friction with the surface and their tangential velocity, M_fric. However, as the line of action of rebound will not always act through the spheroid centroid, a spheroid will experience an additional moment, M_rebound. This moment depends entirely on the normal component of impulse as F_rebound is always normal to the wall and hence couples $\mathrm{CoR_n}$ and Ω. This is shown by comparing the magnitude and location of the maxima and minima from Figures 7b and 7c. This leads to a significant increase in the magnitude of angular velocity where the sign varies depending on the orientation angle, rotating both clockwise and anti-clockwise where an equivalent sphere rotates only clockwise.

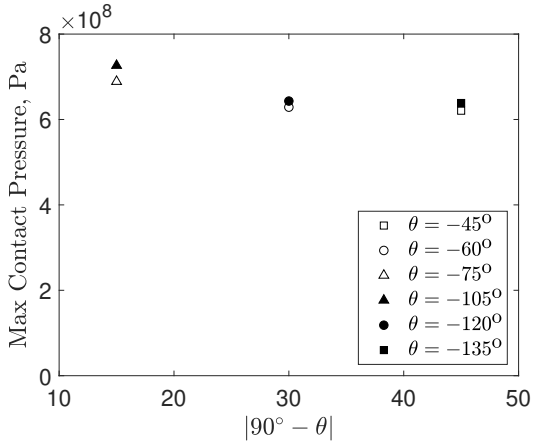

Figure 8: Contact patch maximum surface pressure for collision pairs symmetrical about $\theta = 90°$ for a collision where $\theta_i = 45°$

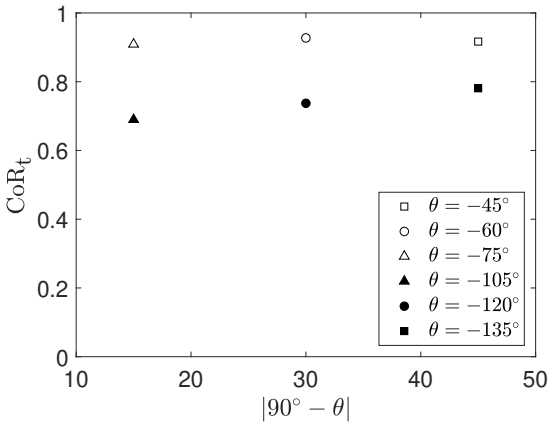

Figure 9: Tangential coefficient of restitution for collision pairs symmetrical about $\theta = 90°$ for a collision where $\theta_i = 45°$

In Figure 7d, M_{rebound} opposes M_{fric} however where $-90° < \theta < 0$ they will act in the same direction. This explains the greater magnitude of the angular velocities where $\theta > -90°$ in Figure 7c. Figure 7b also shows that there is almost always a decrease in $\mathrm{CoR_n}$ compared to the equivalent spherical case. Where $\mathrm{CoR_n} = 0$, the direction of the spheroid centroid velocity is still towards the wall following the first collision as the centroid pivots around the contact patch. The reduction in $\mathrm{CoR_n}$ will increase the time spent by the particle in the surface boundary layer. Combined with the increased magnitude and changing sign of Ω, and the trend of increasing $\mathrm{CoR_t}$ above the equivalent spherical value, discussed later, the rebound trajectory of a spheroid is more susceptible to the influence of the Magnus force as described by Gaskell et al. (2020).

The contributive or opposing moments also explain the smaller peak of $\mathrm{CoR_t}$ in Figure 7a where $-180° < \theta < -90°$, as M_{fric} acts to increase surface pressure and hence friction. This is analogous to the "self-servo" effect observed in drum brakes. Conversely, where $-90° < \theta < 0$, M_{fric} acts to lift the contact patch away from the surface. This is shown by Figures 8 and 9 where geometrically similar collisions with the same angular displacement from $\theta = 90°$, e.g. $85°$ and $95°$, have higher maximum surface pressures where $\theta < -90°$. Geometrically similar means, here, that the local surface curvature at the point of contact is the same and the centroid has the same vertical displacement from the collision surface. As friction is the only factor to influence $\mathrm{CoR_t}$, higher surface pressures increase tangential losses.

The locations and magnitude of the $\mathrm{CoR_t}$ maxima in Figure 7a are also explained by Figure 7b through impulse: maximum average normal force will occur when $\mathrm{CoR_n} = 1$. Reductions in $\mathrm{CoR_n}$ will reduce the average normal force at the contact patch and hence tangential friction. Similar trends can be seen when $\theta_i = 5°$ where the $\mathrm{CoR_t}$ ranges between the equivalent spherical value and unity, inversely correlating with the drop in $\mathrm{CoR_n}$. Spheroid collisions normalised by the equivalent spherical values are shown in Figure 10 for $\mathrm{CoR_n}$ and Ω, where the closeness of fit between impingement angles indicates that the underlying collision physics are similar for both cases.

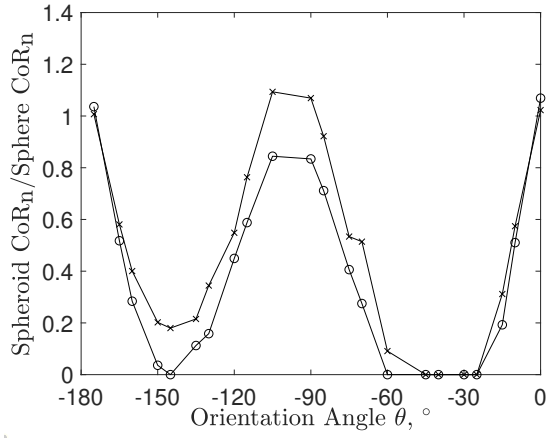

(a) Normal coefficient of restitution

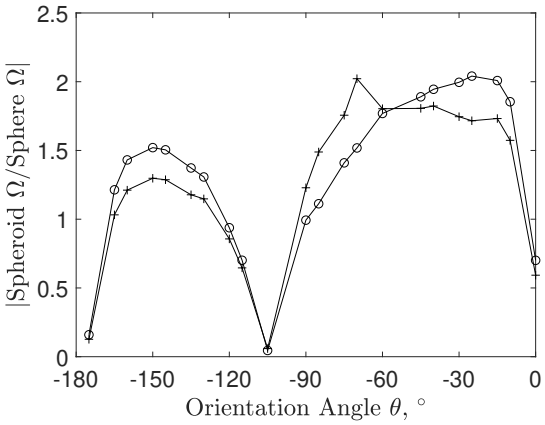

(b) Particle angular velocity magnitude post-rebound

Figure 10: The rebound properties of $\mathrm{AR} = 1.9$ spheroids following their primary collisions where $\theta_\mathrm{i} = 5^\circ$ and $\theta_\mathrm{i} = 45^\circ$, normalised by the value for an equivalent sphere

Following a primary collision, the rebound of spheroids vary significantly from the rebound of spheres. Tangential coefficient of restitution varies between the equivalent spherical value and unity, with average and maximum increases of 20% and 50% for the $\theta = 45^\circ$ cases, excluding cases where second bounces occur. $\mathrm{CoR_n}$ is lower than the equivalent spherical value with a maximum decrease of 84%. Linear kinetic energy is transferred to angular kinetic energy, resulting in angular velocities up to twice as large as those of spheres and often rotating in the opposite direction. Collision physics for normal rebound and angular velocity appear similar for different impingement angles, when normalised by the equivalent spherical value.

Secondary Collisions

Directly simulating multiple collisions in FEA is impractical due to the computational time required and the need for mesh refinement at each point of impact. It is also unnecessary in order to capture secondary collisions occurring immediately following the primary collision. For these collisions, additional external forces are not required, and indeed they modify the particle trajectory insignificantly in the time period considered. Therefore they are not modelled. The FEA models the collision until the point of detachment from the model surface. For a secondary collision to occur it is only necessary that the particle rotation about its centroid is sufficient to bring a point on the ellipsoid surface back into contact with the underlying substrate. The likelihood of this changes with changing rotational speed, aspect ratio, initial impact position and velocity vector leaving the surface. Therefore, the normal, tangential and angular velocities of the spheroids following the first bounce are held constant and an explicit time-stepping scheme implemented in Matlab used to predict whether secondary collisions would occur, and at what orientation angle, θ. Secondary impacts were simulated using FEA data from impacts where $\theta_i = 45^\circ$. The plane on which the particle major axis lies is always aligned normal to the wall in these cases, thus modelling the trajectory of the particle cross-section (ellipse) is sufficient to determine exactly the position of secondary impact, where the particle is translated linearly and rotated about its centroid as per the rebound velocity vectors from its primary collision. The model commences at the point of rebound and continues to displace the 2D representation

Table 1: Orientation of particles at the point of secondary impact

Primary θ °	10.0	15.0	25.0	30.0	40.0	45.0	55.0	60.0	135	145	150	160
Secondary θ °	147	158	163	162	158	153	138	124	60.6	34.2	32.2	39.4

of the ellipsoid until either it re-collides with the ground plane or is sufficiently far from the surface that it will not re-collide. This allows predictions of whether a secondary bounce will occur in addition to providing the particle orientation at the point of re-collision. A timestep sensitivity study confirmed that $\mathcal{O}(10^3)$ timesteps adequately resolved particle motion. The results of this model are shown in Table 1 using inputs from Figure 7, with only those that re-impacted the wall shown. New FEA simulations were performed with the rebound angular, normal and tangential velocities shown in Figure 7 using the orientation angles in Table 1. The same computational setup as as first bounce simulations was used with results shown in Figure 11. Note that the coefficients of restitution and orientation angles shown are with respect to particle velocities and orientation prior to the first collision.

Particles experience a transfer between linear and angular kinetic energies during their primary collisions, as explained previously. From Figures 11b and 11c, this linear kinetic energy is recovered during a secondary collision with the magnitude of angular velocities following the second rebound smaller than the equivalent spherical value and that of the primary rebound. This results in a higher $\mathrm{CoR_n}$ than a first collision alone. Therefore, the magnitude of angular velocity may be between 52% greater ($\theta = -70°$) and 95% lower ($\theta = -105°$) than an equivalent sphere when considering first and second bounces. If all linear kinetic energy transferred to angular kinetic energy is recovered, it might be expected that the angular velocity would be the same as the spherical value given that only friction would influence Ω, as for a sphere. However, as angular velocity due to friction is derived from tangential impulse, increased $\mathrm{CoR_t}$ implies reduced friction and hence explains the lower angular velocites compared to an equivalent sphere.

Where secondary bounces occur, angular kinetic energy derived from the normal impulse of the first collision will be recovered and lead to a $\mathrm{CoR_n}$ similar to that of a sphere. Contact patch friction and therefore $\mathrm{CoR_t}$ is largely unaffected by incoming angular velocity and hence is similar to that of a primary impact. The magnitude of angular velocity following a secondary collision is lower than the equivalent spherical value and that of a primary collision. The greatest overall reduction of $\mathrm{CoR_n}$ in combined primary and secondary collisions is 84% at $\theta = -130°$. Analysis of the second bounce FEA simulations showed that no tertiary collisions occurred.

CONCLUSIONS

The rebound of a spheroid with $AR = 1.9$, broadly representative of an atmospheric particulate that may enter a gas turbine, varies significantly from that of an equivalent sphere. Considering the combined first and second bounces, the $\mathrm{CoR_n}$ may be up to 84% lower than the equivalent spherical value while the $\mathrm{CoR_t}$ may be up to 50% greater. The trajectory following both primary and secondary impacts will have a $\mathrm{CoR_t}$ higher than the equivalent spherical value but

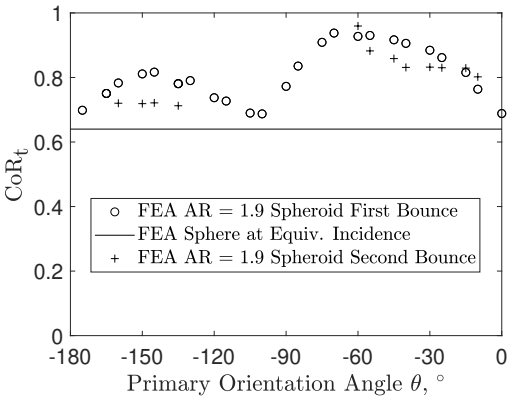

(a) Tangential coefficient of restitution

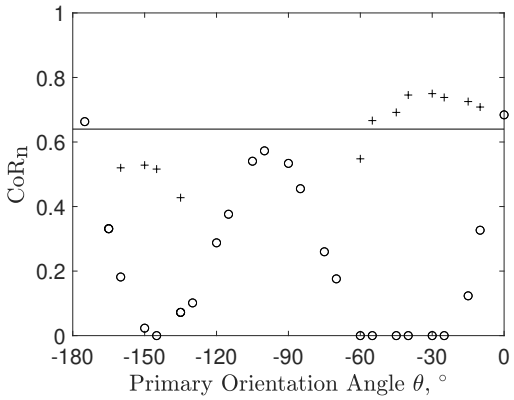

(b) Normal coefficient of restitution

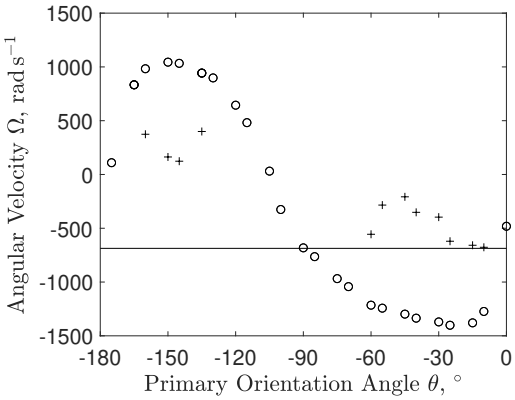

(c) Rebound angular velocity magnitude

Figure 11: Rebound properties of $\mathrm{AR} = 1.9$ spheroids during primary and combined primary-secondary collisions. $\theta_\mathrm{i} = 45^\circ$ prior to the first collision

below unity, as unlike the coupling between $\mathrm{CoR_n}$ and Ω, tangential impulse is only affected by friction. If only one impact with the wall occurs, the normal velocity of the particle during rebound is likely to be significantly lower than that of an equivalent sphere while the occurrence of a second impact recovers angular kinetic energy and leads to a $\mathrm{CoR_n}$ similar to an equivalent sphere. Particle angular velocity following any number of impacts is likely to be affected by non-sphericity, changing sign with a magnitude between 152% and 5% of the equivalent spherical value. This affects particle trajectory and the likelihood of subsequent deposition through the Magnus force. Normalisation of the results showed no fundamental differences between the collision dynamics of particles at different impingement angles. This suggests a means by which a surrogate model for non sphericity might be implemented in future.

The normal and tangential aspects of spheroidal collision dynamics are highly coupled, presenting challenges when developing bounce-stick models for non-spherical particles. Whether particles re-collide immediately with the surface was found using a simple time-stepping scheme. Indeed, predicting whether a second bounce occurs and its effects are crucial to accurately predicting particle downstream trajectory. The results presented here provide a sensitivity analysis of particle rebound to non-sphericity and can also be used as validation data for future bounce-

stick models. The rebound trajectories shown here demonstrate that particle non-sphericity must be considered in bounce-stick models to accurately predict downstream deposition.

ACKNOWLEDGEMENTS

The authors would like to gratefully acknowledge the financial support and collaboration of Rolls-Royce Plc and the ATI through the MALIT programme, and the funding of the lead author through the EPSRC and the Centre for Doctoral Training in Gas Turbine Aerodynamics.

REFERENCES

Bons, J. P., R. Prenter, and S. Whitaker (2017). "A Simple Physics-Based Model for Particle Rebound and Deposition in Turbomachinery". In: *Journal of Turbomachinery* 139.8, p. 081009. DOI: 10.1115/1.4035921.

Brach, Raymond M. and Patrick F. Dunn (1992). "A Mathematical Model of the Impact and Adhesion of Microsphers". In: *Aerosol Science and Technology* 16.1, 51â64. DOI: 10.1080/02786829208959537.

Chou, Cedric et al. (2008). "Size distribution, shape, and composition of mineral dust aerosols collected during the African Monsoon Multidisciplinary Analysis Special Observation Period 0: Dust and Biomass-Burning Experiment field campaign in Niger, January 2006". In: *Journal of Geophysical Research* 113. DOI: 10.1029/2008jd009897.

Clarkson, Rory J, Elizabeth Je Majewicz, and Peter Mack (2016). "A re-evaluation of the 2010 quantitative understanding of the effects volcanic ash has on gas turbine engines". In: *Proceedings of the Institution of Mechanical Engineers, Part G: Journal of Aerospace Engineering* 230.12, 2274â2291. DOI: 10.1177/0954410015623372.

Dunn, Michael G. (2012). "Operation of Gas Turbine Engines in an Environment Contaminated With Volcanic Ash". In: *Journal of Turbomachinery* 134.5, p. 051001.

Gaskell, Jack G. et al. (2020). "Collision-Induced Rotation and the Magnus Force on Particulates". In: *AIAA Aviation 2020 Forum*. DOI: 10.2514/6.2020-2820.

Gorham, D.A. and A.H. Kharaz (2000). "The measurement of particle rebound characteristics". In: *Powder Technology* 112.3, 193â202. DOI: 10.1016/s0032-5910(00)00293-x.

Jie, Yucheng et al. (2019). "Preferential orientation of tracer spheroids in turbulent channel flow". In: *Theoretical and Applied Mechanics Letters* 9.3, 212â214. DOI: 10.1016/j.taml.2019.03.010.

Marchioli, Cristian, Marco Fantoni, and Alfredo Soldati (2010). "Orientation, distribution, and deposition of elongated, inertial fibers in turbulent channel flow". In: *Physics of Fluids* 22.3, p. 033301. DOI: 10.1063/1.3328874.

Reid, Elizabeth A. (2003). "Characterization of African dust transported to Puerto Rico by individual particle and size segregated bulk analysis". In: *Journal of Geophysical Research* 108.D19. DOI: 10.1029/2002jd002935.

Whitaker, Steven M. and Jeffrey P. Bons (2018). "An Improved Particle Impact Model by Accounting for Rate of Strain and Stochastic Rebound". In: *Volume 2D: Turbomachinery*. DOI: 10.1115/gt2018-77158.

Wynn, E.J.W. (2009). "Simulations of rebound of an elastic ellipsoid colliding with a plane". In: *Powder Technology* 196.1, 62â73. DOI: 10.1016/j.powtec.2009.07.004.

Yu, Kuahai and Danesh Tafti (2019). "Size- and Temperature-Dependent Collision and Deposition Model for Micron-Sized Sand Particles". In: *Journal of Turbomachinery* 141.3, p. 031001. DOI: 10.1115/1.4042215.